

Measurement of $D^{*\pm}$ production in deep inelastic $e^\pm p$ scattering at HERA

ZEUS Collaboration

Abstract

Inclusive production of $D^{*\pm}$ (2010) mesons in deep inelastic scattering has been measured with the ZEUS detector at HERA using an integrated luminosity of 81.9 pb^{-1} . The decay channel $D^{*+} \rightarrow D^0 \pi^+$ with $D^0 \rightarrow K^- \pi^+$ and corresponding antiparticle decay were used to identify D^* mesons. Differential D^* cross sections with $1.5 < Q^2 < 1000 \text{ GeV}^2$ and $0.02 < y < 0.7$ in the kinematic region $1.5 < p_T(D^*) < 15 \text{ GeV}$ and $|\eta(D^*)| < 1.5$ are compared to different QCD calculations incorporating different parameterisations of the parton densities in the proton. The data show sensitivity to the gluon distribution in the proton and are reasonably well described by next-to-leading-order QCD with the ZEUS NLO QCD fit used as the input parton density in the proton. The observed cross section is extrapolated to the full kinematic region in $p_T(D^*)$ and $\eta(D^*)$ in order to determine the open charm contribution, $F_2^{c\bar{c}}(x, Q^2)$, to the proton structure function. Since at low Q^2 , the uncertainties on the data are comparable to those from the PDF fit the measured differential cross sections in y and Q^2 should be used in future fits to constrain the gluon density.

1 Introduction

Charm quarks are produced copiously in deep inelastic scattering (DIS) at HERA. At sufficiently high photon virtualities, Q^2 , the production of charm quarks has been measured to constitute up to 30% of the total cross section [1, 2]. Previous measurements of D^* cross sections [1–4] indicate that the production of charm quarks in DIS in the range $1 < Q^2 < 600 \text{ GeV}^2$ is consistent with Quantum Chromodynamics (QCD) calculations where charm is produced through the boson-gluon-fusion (BGF) mechanism. This implies the charm cross section is directly sensitive to the gluon density in the proton.

In this paper measurements of the D^* cross section are presented with improved precision and in a kinematic region extending to higher Q^2 than previous ZEUS results [1]. Single differential cross sections have been measured as a function of Q^2 and the Bjorken scaling variable, x . Cross sections have also been measured in two Q^2 ranges as a function of transverse momentum, $p_T(D^*)$, and pseudorapidity, $\eta(D^*)$, of the D^* meson. The cross sections are compared to leading-logarithmic Monte Carlo (MC) predictions and to a next-to-leading-order (NLO) QCD calculation using different parton density functions (PDFs) in the proton. In particular, the data are compared to calculations using the recent ZEUS NLO QCD fit [5], in which the parton densities in the proton are parameterised by performing fits to inclusive DIS measurements from ZEUS and fixed-target experiments. The cross section measurements are used to extract the charm contribution, $F_2^{c\bar{c}}$, to the proton structure function, F_2 .

2 Experimental set-up

The analysis was performed with data taken from 1998 to 2000, when HERA collided electrons or positrons with energy $E_e = 27.5 \text{ GeV}$ with protons of energy $E_p = 920 \text{ GeV}$. The results are based on e^-p and e^+p samples corresponding to integrated luminosities of $16.7 \pm 0.3 \text{ pb}^{-1}$ and $65.2 \pm 1.5 \text{ pb}^{-1}$, respectively.¹

A detailed description of the ZEUS detector can be found elsewhere [6]. A brief outline of the components that are most relevant for this analysis is given below.

Charged particles are tracked in the central tracking detector (CTD) [7], which operates in a magnetic field of 1.43 T provided by a thin superconducting solenoid. The CTD consists of 72 cylindrical drift chamber layers, organised in nine superlayers covering the

¹ Hereafter, both electrons and positrons are referred to as electrons, unless explicitly stated otherwise.

polar-angle² region $15^\circ < \theta < 164^\circ$. The transverse-momentum resolution for full-length tracks is $\sigma(p_T)/p_T = 0.0058p_T \oplus 0.0065 \oplus 0.0014/p_T$, with p_T in GeV.

The high-resolution uranium–scintillator calorimeter (CAL) [8] consists of three parts: the forward (FCAL), the barrel (BCAL) and the rear (RCAL) calorimeters. Each part is subdivided transversely into towers and longitudinally into one electromagnetic section (EMC) and either one (in RCAL) or two (in BCAL and FCAL) hadronic sections (HAC). The smallest subdivision of the calorimeter is called a cell. The CAL energy resolutions, as measured under test-beam conditions, are $\sigma(E)/E = 0.18/\sqrt{E}$ for electrons and $\sigma(E)/E = 0.35/\sqrt{E}$ for hadrons, with E in GeV.

Presamplers (PRES) [9] are mounted in front of FCAL, BCAL and RCAL. They consist of scintillator tiles that detect particles originating from showers in the material between the interaction point and the calorimeter. This information was used to correct the energy of the scattered electron. The position of electrons scattered close to the electron beam direction is determined by a scintillator strip detector (SRTD) [10]. The SRTD signals resolve single minimum-ionising particles and provide a transverse position resolution of 3 mm.

The luminosity was measured from the rate of the bremsstrahlung process $ep \rightarrow e\gamma p$, where the photon was measured in a lead–scintillator calorimeter [11] placed in the HERA tunnel at $Z = -107$ m.

A three-level trigger system was used to select events online [6, 12]. At the third level, events with both a reconstructed D^* candidate and a scattered-electron candidate were kept for further analysis. The efficiency of the online D^* reconstruction, determined relative to an inclusive DIS trigger, was generally above 95%.

3 Theoretical predictions

Many models of charm production in DIS exist which have very different theoretical bases. To thoroughly test the measurements of D^* production presented in this paper, predictions need to be able to calculate the cross sections in the given kinematic region. The calculation used in this paper to compare with the measured cross sections is based on NLO QCD as described in Section 3.1. Other models which generally only predict the total cross section cannot be compared with the data and are briefly discussed in Section 3.3.

² The ZEUS coordinate system is a right-handed Cartesian system, with the Z axis pointing in the proton beam direction, referred to as the “forward direction”, and the X axis pointing left towards the centre of HERA. The coordinate origin is at the nominal interaction point.

3.1 NLO QCD calculations

The NLO predictions for $c\bar{c}$ cross sections were obtained using the HVQDIS program [13] based on the so-called fixed-flavour-number scheme (FFNS). In this scheme, only light quarks (u, d, s) are included in the initial-state proton as partons whose distributions obey the DGLAP equations [14] and the $c\bar{c}$ is produced via the BGF mechanism [15] with NLO corrections [16]. The presence of the two large scales, Q^2 and m_c^2 , can spoil the convergence of the perturbative series because the neglected terms of orders higher than α_s^2 contain $\log(Q^2/m_c^2)$ factors which can become large. Therefore, the results of HVQDIS are expected to be most accurate at $Q^2 \approx m_c^2$ and to become less reliable when $Q^2 \gg m_c^2$.

The following inputs have been used to obtain the predictions for D^* production at NLO using the program HVQDIS. The recent ZEUS NLO QCD global fit [5] to structure-function data was used as the parametrisation of the proton PDFs. This fit was repeated [17] in the FFNS, in which the PDF has three active quark flavours in the proton and $\Lambda_{\text{QCD}}^{(3)}$ set to 0.363 GeV. In this fit, the mass of the charm quark was set to 1.35 GeV; this was therefore used in the calculation of the predictions. The renormalisation and factorisation scales were set to $\mu = \sqrt{Q^2 + 4m_c^2}$. The charm fragmentation to a D^* is carried out using the Peterson function [18]. The hadronisation fraction, $f(c \rightarrow D^*)$, was set to 0.235 [19] and the Peterson parameter, ϵ , was set to 0.035 [20]. The hadronisation fraction was taken from combined e^+e^- measurements. However, the production cross section for charmonium states at HERA is larger than in high-energy e^+e^- collisions. The effect of J/ψ production on the hadronisation fraction was estimated from data [21, 22] to be about 2% and was neglected.

As an alternative to the Peterson hadronisation scheme, corrections were applied to the partons in the NLO calculation using the AROMA MC program [23] (see Section 3.2) which uses the Lund string fragmentation [24] and leading-logarithmic parton showers. This was applied on a bin-by-bin basis to the NLO calculation for each cross section measured, according to the formula $d\sigma(D^*)_{\text{NLO+MC}} = d\sigma(c\bar{c})_{\text{NLO}} \cdot C_{\text{had}}$ where $C_{\text{had}} = d\sigma(D^*)_{\text{MC}}/d\sigma(c\bar{c})_{\text{MC}}$. The shapes of the differential cross sections calculated at the parton level of the AROMA model agreed reasonably well with those calculated from the HVQDIS program. The difference in using this hadronisation correction and that using the Peterson fragmentation is discussed in Sections 9 and 10.

To estimate the contribution of beauty production, the NLO calculation and hadronisation from the MC were combined, using $d\sigma(b \rightarrow D^*)_{\text{NLO+MC}} = d\sigma(b\bar{b})_{\text{NLO}} \cdot C_{\text{had}}$ where $C_{\text{had}} = d\sigma(b \rightarrow D^*)_{\text{MC}}/d\sigma(b\bar{b})_{\text{MC}}$. The ZEUS NLO fit was used as the proton PDF, with the mass set in the fit, $m_b = 4.3$ GeV, used in the HVQDIS program and μ set to $\sqrt{Q^2 + 4m_b^2}$.

An alternate scheme to describe charm production in QCD is the variable-flavour-number scheme (VFNS) [25, 26]. In this scheme, an attempt is made to treat the heavy quarks

correctly for all Q^2 . Therefore, at low Q^2 , charm is produced dynamically through the BGF process as in the FFNS, whereas at higher Q^2 , heavy-quark parton densities are introduced. The transition between the two extremes is treated in different ways by different authors [25, 26]. Predictions from this scheme are, however, only available for the total cross section. The ZEUS NLO QCD fit has been performed in this scheme using the formalism of Roberts and Thorne [27, 28]. No full calculation of D^* production in the VFNS is available.

3.2 Monte Carlo models of charm production

The MC programs AROMA and CASCADE [29] were also compared with the measured differential cross sections. In the AROMA MC program, charm is produced via the BGF process. Higher-order QCD effects are simulated in the leading-logarithmic approximation with initial- and final-state radiation obeying DGLAP evolution. The mass of the charm quark was set to 1.5 GeV and the proton PDF chosen was CTEQ5F3 [30]. The CASCADE MC model takes a different approach to the generation of the hard sub-process, in which heavy quark production is simulated in the framework of the semi-hard or k_T -factorisation approach [31, 32]. The matrix element used in CASCADE is the off-shell LO BGF process [31, 33]. The CASCADE initial-state radiation is based on CCFM evolution [34], which includes $\ln(1/x)$ terms in the perturbative expansion in addition to the $\ln Q^2$ terms used in DGLAP evolution. To simulate final-state radiation, CASCADE uses PYTHIA 5.7 [35]. The cross section is calculated by convoluting the off-shell BGF matrix element with the unintegrated gluon density of the proton obtained from the CCFM fit to the HERA F_2 data [36] with $m_c = 1.5$ GeV. For both AROMA and CASCADE, the Lund string model is used for the fragmentation into hadrons and $f(c \rightarrow D^*)$ was set to 0.235.

3.3 Other predictions of charm production

Several models of charm production [37] were compared in the kinematic range measured in this paper. As many only predict total cross sections, the comparison was performed for $F_2^{c\bar{c}}$. In this kinematic range, all models showed similar trends; the differences were typically less than 20%. The precision of the current data is not sufficient to distinguish between these models. The extraction of $F_2^{c\bar{c}}$ is also a model-dependent measurement and so a comparison of the other models with the data is not strictly valid. The extraction is performed with the FFNS predictions and, therefore, the final data are only comparable to these predictions. For a valid comparison of the data with the predictions, the models should be able to calculate the dynamics of the production mechanism.

4 Kinematic reconstruction and event selection

The kinematic variables, Q^2 , x and the fraction of the electron energy transferred to the proton in its rest frame, y , can be reconstructed in the ZEUS detector using a variety of methods, whose accuracy depends on the variable of interest and its range:

- for the electron method (specified with the subscript e), the measured energy and angle of the scattered lepton are used;
- the double angle (DA) method [38] relies on the angles of the scattered lepton and the hadronic energy flow;
- the Jacquet-Blondel (JB) method [39] is based entirely on measurements of the hadronic system;
- the Σ -method [40] uses both the scattered-lepton energy and measurements of the hadronic system.

The reconstruction of Q^2 and x was performed using the Σ -method, since it has better resolution at low Q^2 than the DA method. At high Q^2 , the Σ -method and the DA method are similar, and both have better resolution than the electron method.

The events were selected [1,41] by the following cuts:

- the scattered electron was identified using a neural-network procedure [42]. Its energy, $E_{e'}$, was required to be larger than 10 GeV;
- $y_e \leq 0.95$;
- $y_{\text{JB}} \geq 0.02$;
- $40 \leq \delta \leq 60$ GeV, where $\delta = \sum E_i(1 - \cos \theta_i)$, E_i is the energy of the calorimeter cell i and the sum runs over all cells;
- a primary vertex position determined from the tracks fitted to the vertex in the range $|Z_{\text{vertex}}| < 50$ cm;
- the impact point (X, Y) of the scattered lepton on the RCAL must lie outside the region 26×14 cm² centred on $X = Y = 0$.

The kinematic region for DIS events was $1.5 < Q^2 < 1000$ GeV² and $0.02 < y < 0.7$.

5 Selection of D^* candidates

The D^* mesons were identified using the decay channel $D^{*+} \rightarrow D^0 \pi_s^+$ with the subsequent decay $D^0 \rightarrow K^- \pi^+$ and the corresponding antiparticle decay, where π_s^+ refers to a low-momentum (“slow”) pion accompanying the D^0 .

Charged tracks measured by the CTD and assigned to the primary event vertex were selected. The transverse momentum was required to be greater than 0.12 GeV. Each track was required to reach at least the third superlayer of the CTD. These restrictions ensured that the track acceptance and momentum resolution were high. Tracks in the CTD with opposite charges and transverse momenta $p_T > 0.4$ GeV were combined in pairs to form D^0 candidates. The tracks were alternately assigned the masses of a kaon and a pion and the invariant mass of the pair, $M_{K\pi}$, was found. Each additional track, with charge opposite to that of the kaon track, was assigned the pion mass and combined with the D^0 -meson candidate to form a D^* candidate.

The signal regions for the reconstructed masses, $M(D^0)$ and $\Delta M = (M_{K\pi\pi_s} - M_{K\pi})$, were $1.80 < M(D^0) < 1.92$ GeV and $0.143 < \Delta M < 0.148$ GeV, respectively. To allow the background to be determined, D^0 candidates with wrong-sign combinations, in which both tracks forming the D^0 candidates have the same charge and the third track has the opposite charge, were also retained. The same kinematic restrictions were applied as for those D^0 candidates with correct-charge combinations.

The kinematic region for D^* candidates was $1.5 < p_T(D^*) < 15$ GeV and $|\eta(D^*)| < 1.5$. Figure 1 shows the ΔM distribution for the D^* candidates together with the background from the wrong-charge combinations. The fit to the distribution has the form

$$F = p_1 \cdot \exp\left(-0.5 \cdot x^{1+\frac{1}{1+0.5x}}\right) + p_4 \cdot (\Delta M - m_\pi)^{p_5},$$

where $x = |(\Delta M - p_2)/p_3|$, $p_1 - p_5$ are free parameters and m_π is the pion mass. The “modified” Gaussian was used to fit the mass peak since it gave a better χ^2 value than the conventional Gaussian form for a clean MC sample of D^* mesons. The fitted width of 0.75 ± 0.02 MeV is consistent with the experimental resolution. Consistent results were also found for the e^+p and e^-p data separately.

The number of D^* candidates determined after subtracting the background estimated from the wrong-charge sample was 5545 ± 129 . The normalisation factor of the wrong-charge sample was determined as the ratio of events with correct-charge combinations to wrong-charge combinations in the region $150 < \Delta M < 165$ MeV. This factor is compatible with 1 for both e^-p and e^+p data. The normalisation factors were determined for each bin in order to calculate the differential cross sections using the background-subtraction method.

6 Acceptance corrections

The acceptances were calculated using the RAPGAP 2.08 [43] and HERWIG 6.1 [44] MC models. The RAPGAP MC model was interfaced with HERACLES 4.5 [45] in order to

incorporate first-order electroweak corrections. The generated events were then passed through a full simulation of the detector, separately for e^-p and e^+p running, using GEANT 3.13 [46] and processed and selected with the same programs as used for the real data.

The MC models RAPGAP and HERWIG were used to produce charm by the BGF process only. The GRV94-LO [47] PDF for the proton was used, and the charm-quark mass was set to 1.5 GeV. The HERWIG MC contains leading-logarithmic parton showers whereas for RAPGAP MC, the colour-dipole model [48] as implemented in ARIADNE 4.03 [48] was used to simulate QCD radiation. Charm fragmentation is implemented using either the Lund string fragmentation (RAPGAP) or a cluster fragmentation [49] model (HERWIG).

Figure 2 shows distributions of DIS variables for D^* events (after background subtraction) for data compared to detector-level RAPGAP predictions. The distributions, which are normalised to unit area, are shown separately for two Q^2 intervals: $1.5 < Q^2 < 1000 \text{ GeV}^2$ and $40 < Q^2 < 1000 \text{ GeV}^2$. The RAPGAP predictions are in good agreement with the data for both the scattered-lepton and hadronic variables. The description is similarly good for the two Q^2 ranges. The good description of the data gives confidence in the use of the RAPGAP MC to correct the data for detector effects. The HERWIG MC gives a similarly good description of the data (not shown) and is used to estimate the systematic uncertainty arising from the model in the correction procedure as described in Section 8.

The cross sections for a given observable Y were determined using

$$\frac{d\sigma}{dY} = \frac{N}{A \cdot \mathcal{L} \cdot B \cdot \Delta Y},$$

where N is the number of D^* events in a bin of size ΔY , A is the acceptance (which takes into account migrations, efficiencies and radiative effects for that bin) and \mathcal{L} is the integrated luminosity. The product, B , of the appropriate branching ratios for the D^* and D^0 was set to $(2.57 \pm 0.06)\%$ [50].

7 D^* rates in e^-p and e^+p interactions

The D^* rates, $r = N/\mathcal{L}$, in the e^-p data set was systematically higher than that in the e^+p data set. This difference increases with Q^2 ; for example, the ratio of the rates, r^{e^-p}/r^{e^+p} , is equal to 1.12 ± 0.06 for $1.5 < Q^2 < 1000 \text{ GeV}^2$, while for $40 < Q^2 < 1000 \text{ GeV}^2$ it is 1.67 ± 0.21 (only statistical errors are given). Such a difference is not expected in this Q^2 range from known physics processes.

A detailed study of systematic effects was performed to understand if there were any instrumental effects which could account for the difference in the two data sets. The rate

for the wrong-charge background under the D^* mass peak in e^-p data agreed well with the wrong-charge rate in e^+p data. For example, for $Q^2 > 40 \text{ GeV}^2$, where the largest difference exists, the ratio of the rates for wrong-charge track combinations in e^-p and e^+p data is 0.95 ± 0.09 . For both e^-p and e^+p interactions, the number of D^{*+} candidates was consistent with the number of D^{*-} for the entire Q^2 range studied. Different reconstruction methods, cuts, background-subtraction methods and the time dependence of the difference were also investigated. None of these checks gave an indication of the source of the observed difference between the D^* rates in e^-p and e^+p for $Q^2 > 40 \text{ GeV}^2$. The cross sections were measured separately for e^-p and e^+p data and are discussed in Section 9. The difference in observed rate is assumed to be a statistical fluctuation. Therefore, the two sets of data were combined.

8 Experimental and theoretical uncertainties

8.1 Experimental uncertainties

The systematic uncertainties of the measured cross sections were determined by changing the selection cuts or the analysis procedure in turn and repeating the extraction of the cross sections [51]. The following systematic studies have been carried out (the resulting uncertainty on the total cross section is given in parentheses):

- event reconstruction and selection ($^{+2.3}_{-0.7}\%$). The following systematic checks were performed for this category:
 - the cut on y_e was changed to $y_e \leq 0.90$;
 - the cut on y_{JB} was changed to $y_{JB} \geq 0.03$;
 - the cut on δ was changed to $42 \leq \delta \leq 57 \text{ GeV}$;
 - the cut on the $|Z_{\text{vertex}}|$ was changed to $|Z_{\text{vertex}}| < 45 \text{ cm}$;
 - the cut on $E_{e'}$ was changed to $E_{e'} > 11 \text{ GeV}$;
 - the cut on the position of the scattered lepton in the RCAL was raised by 1 cm;
 - the electron method was used, except for cases when the scattered-lepton track was reconstructed by the CTD. In the latter case, the DA method, which has the best resolution at high Q^2 , was used;
 - the energy of the scattered electron was raised and lowered by 1% in the MC only to account for the uncertainty in the CAL energy scale;
 - the energy of the hadronic system was raised and lowered by 3% in the MC only to account for the uncertainty in the hadronic CAL energy scale.

- uncertainties related to the D^* reconstruction ($^{+2.9}_{-1.6}\%$). The following systematic checks were performed for this category:
 - tracks were required to have $|\eta| < 1.75$, in addition to the requirement on the number of superlayers;
 - the cut on the minimum transverse momentum for the π and K candidates was raised and lowered by 0.1 GeV;
 - the cut on the minimum transverse momentum for the π_s was raised and lowered by 0.02 GeV;
 - the signal region for the $M(D^0)$ was widened and narrowed symmetrically around the centre by 0.01 GeV;
 - the signal region for the ΔM was widened and narrowed symmetrically around the centre by 0.003 GeV.
- the acceptance was determined using HERWIG instead of RAPGAP (-2.7%).
- the uncertainty of 2.2% in the luminosity measurement;

The cross section obtained using the fit was found to be in good agreement with that when subtracting the background using the wrong-charge candidates. These estimations were also made in each bin in which the differential cross sections were measured. The overall systematic uncertainty was determined by adding the above uncertainties in quadrature. The normalisation uncertainties due to the luminosity-measurement error, and those due to the D^* and D^0 decay branching ratios [50] were not included in the systematic uncertainties for the differential cross sections.

8.2 Theoretical uncertainties

The NLO QCD predictions for D^* production are affected by the systematic uncertainties listed below. Typical values for the systematic uncertainty are quoted for the total cross section:

- the proton PDF. The CTEQ5F3 and GRV98-HO [52] PDFs were used to check the sensitivity to different parameterisations of the gluon density in the proton. The appropriate masses used in the fit to determine the PDF were also used in HVQDIS, i.e. 1.3 GeV for CTEQ5F3 and 1.4 GeV for GRV98-HO. The change in the cross section was $+1.4\%$ using CTEQ5F3 and -16% using GRV98-HO;
- the mass of the charm quark ($^{+9.7}_{-9.1}\%$). The charm mass was changed consistently in the PDF fit and in HVQDIS by ∓ 0.15 GeV. The largest effect was at low $p_T(D^*)$;

- the renormalisation and factorisation scale, μ ($^{+40}_{-1}\%$). The scale was changed by a factor of 0.5 and 2; another scale, $2m_c$, was also used [13]. The maximum of $\sqrt{Q^2/4 + m_c^2}$ and $2m_c$ as a function of Q^2 was taken as the scale to estimate the upward uncertainty;
- the ZEUS PDF uncertainties propagated from the experimental uncertainties of the fitted data ($\pm 5\%$). The change in the cross section was independent of the kinematic region;
- uncertainty in the fragmentation ($^{+6}_{-4}\%$). The parameter ϵ in the Peterson fragmentation function was changed by ± 0.015 .

The first source of systematic uncertainty is shown separately in the figures. The last four were added in quadrature and displayed as a band in the figures. An additional normalisation uncertainty of 3% [19] on the hadronisation fraction $f(c \rightarrow D^*)$ is not shown.

9 Cross-section measurements

9.1 Visible cross sections

The overall acceptance after applying the selection criteria described in Sections 4 and 5 for $1.5 < Q^2 < 1000 \text{ GeV}^2$, $0.02 < y < 0.7$, $1.5 < p_T(D^*) < 15 \text{ GeV}$ and $|\eta(D^*)| < 1.5$ calculated with RAPGAP is 31%, both for e^-p and e^+p data. The total cross sections in the same region are:

$$\sigma(e^-p \rightarrow e^- D^* X) = 9.37 \pm 0.44(\text{stat.})_{-0.45}^{+0.59}(\text{syst.}) \pm 0.24(\text{BR}) \text{ nb};$$

$$\sigma(e^+p \rightarrow e^+ D^* X) = 8.20 \pm 0.22(\text{stat.})_{-0.34}^{+0.39}(\text{syst.}) \pm 0.21(\text{BR}) \text{ nb},$$

where the final uncertainty arises from the uncertainty on the branching ratios for the D^* and D^0 . The D^* cross section for e^+p data is consistent with the previously published result [1] obtained at a proton beam energy of 820 GeV. According to HVQDIS, a 5% increase in the D^* cross section is expected when the proton energy increases from 820 to 920 GeV. The cross section obtained from the combined sample is:

$$\sigma(e^\pm p \rightarrow e^\pm D^* X) = 8.44 \pm 0.20(\text{stat.})_{-0.32}^{+0.37}(\text{syst.}) \pm 0.22(\text{BR}) \text{ nb}.$$

The prediction from the HVQDIS program is $8.53_{-0.96}^{+1.09} \text{ nb}$, in good agreement with the data. The uncertainty in the HVQDIS prediction arises from the sources discussed in

Section 8.2 and is about three times the size of the uncertainty in the measurement. A contribution to the total cross sections arises from D^* mesons produced in $b\bar{b}$ events. The D^* cross section arising from $b\bar{b}$ production was estimated, as described in Section 3, to be 0.23 nb for $Q^2 > 1.5 \text{ GeV}^2$. The measured differential cross sections include a component from beauty production. Therefore, all NLO predictions include a $b\bar{b}$ contribution calculated in each bin. For the extraction of F_2^{cc} , the predicted value of $b\bar{b}$ production was subtracted from the data.

9.2 Differential cross-section measurements

The differential D^* cross sections as a function of Q^2 , x , $p_T(D^*)$ and $\eta(D^*)$ for the combined e^-p and e^+p data samples are shown in Fig. 3. The cross sections in Q^2 and x both fall by about four orders of magnitude in the measured region. The cross-section $d\sigma/dp_T(D^*)$ falls by two orders of magnitude with increasing $p_T(D^*)$. The cross-section $d\sigma/d\eta(D^*)$ rises with increasing $\eta(D^*)$. The ratio of the e^-p and e^+p cross sections, also shown in Fig. 3, tends to increase with increasing Q^2 and x . Both the NLO calculations and MCs based on LO matrix elements and parton showers do not depend on the charge of the lepton in ep interactions.

The data in Fig. 3 are compared with predictions from the MC generators AROMA and CASCADE. The prediction from AROMA is generally below the data, particularly at low Q^2 and medium to high $p_T(D^*)$. In contrast, the prediction from CASCADE agrees at low Q^2 , but generally lies above the data. Both MC predictions describe the shapes of the cross-sections $d\sigma/dx$ and $d\sigma/d\eta(D^*)$ reasonably well. The uncertainties in these MC predictions are difficult to estimate and may be large.

In Fig. 4, the same data are shown compared with the NLO calculation implemented in the HVQDIS program. The predictions used the default parameter settings as discussed in Section 3 with the uncertainties assessed as described in Section 8.2. Predictions using an alternate PDF, CTEQ5F3, and an alternate hadronisation scheme, using AROMA, are also shown. The differences between the predictions are comparable to the uncertainties in the data demonstrating the sensitivity of this measurement to the gluon distribution in the proton. The ratio of data to theory is displayed for each variable. For the cross sections as a function of Q^2 and x , the NLO predictions give a reasonable description of the data over four orders of magnitude in the cross section. The NLO calculation does, however, exhibit a somewhat different shape, particularly for $d\sigma/dx$, where the NLO is below the data at low x and above the data at high x . For $d\sigma/dQ^2$, the description of the data is similar over the whole range in Q^2 although HVQDIS is expected to be most accurate when $Q^2 \sim m_c^2$. The predictions using CTEQ5F3 instead of the ZEUS NLO fit, or using AROMA for the hadronisation instead of the Peterson function, give better

agreement with the data for the cross-section $d\sigma/dx$.

The cross sections as a function of $p_T(D^*)$ and $\eta(D^*)$ are also reasonably well described by the NLO calculation. The prediction using the ZEUS NLO QCD fit gives a better description than that using CTEQ5F3 (and also better than the prediction using GRV98-HO, not shown), especially for the cross section $d\sigma/d\eta(D^*)$. A better description of $d\sigma/d\eta(D^*)$ is also achieved [53] by using AROMA for the hadronisation, although, in this case, $d\sigma/dp_T(D^*)$ is not so well described. It should be noted that previous publications [1, 2] revealed discrepancies in the forward $\eta(D^*)$ direction which can now be reasonably well described by a recent fit to the proton PDF. The data presented here are practically independent of the data used in the ZEUS NLO PDF fit to inclusive DIS data. Further refinement of NLO QCD fits and even use of these data in future fits may achieve a better description of these data.

Cross sections as a function of $\eta(D^*)$ and $p_T(D^*)$ were also measured for $Q^2 > 40 \text{ GeV}^2$. The combined e^-p and e^+p data samples are shown in Fig. 5 compared with the HVQDIS predictions. The HVQDIS calculation is not necessarily applicable at high Q^2 , however the data are well described. The high Q^2 region is also where the difference in e^-p and e^+p data is most pronounced.

10 Extraction of $F_2^{c\bar{c}}$

The open-charm contribution, $F_2^{c\bar{c}}$, to the proton structure-function F_2 can be defined in terms of the inclusive double-differential $c\bar{c}$ cross section in x and Q^2 by

$$\frac{d^2\sigma^{c\bar{c}}(x, Q^2)}{dx dQ^2} = \frac{2\pi\alpha^2}{xQ^4} \{[1 + (1 - y)^2]F_2^{c\bar{c}}(x, Q^2) - y^2 F_L^{c\bar{c}}(x, Q^2)\}. \quad (1)$$

In this paper, the $c\bar{c}$ cross section is obtained by measuring the D^* production cross section and employing the hadronisation fraction $f(c \rightarrow D^*)$ to derive the total charm cross section. Since only a limited kinematic region is accessible for the measurement of D^* mesons, a prescription for extrapolating to the full kinematic phase space is needed.

Since the structure function varies only slowly, it is assumed to be constant within a given Q^2 and y bin. Thus, the measured $F_2^{c\bar{c}}$ in a bin i is given by

$$F_{2 \text{ meas}}^{c\bar{c}}(x_i, Q_i^2) = \frac{\sigma_{i, \text{meas}}(ep \rightarrow D^* X)}{\sigma_{i, \text{theo}}(ep \rightarrow D^* X)} F_{2 \text{ theo}}^{c\bar{c}}(x_i, Q_i^2), \quad (2)$$

where σ_i are the cross sections in bin i in the measured region of $p_T(D^*)$ and $\eta(D^*)$. The value of $F_{2 \text{ theo}}^{c\bar{c}}$ was calculated from the NLO coefficient functions [5]. The functional form

of $F_{2\text{theo}}^{c\bar{c}}$ was used to quote the results for $F_2^{c\bar{c}}$ at convenient values of x_i and Q_i^2 close to the centre-of-gravity of the bin. In this calculation, the same parton densities, charm mass ($m_c = 1.35$ GeV), and factorisation and renormalisation scales ($\sqrt{4m_c^2 + Q^2}$) have been used as for the HVQDIS calculation of the differential cross sections. The hadronisation was performed using the Peterson fragmentation function.

The beauty contribution was subtracted from the data using the theoretical prediction as described in Section 3. At low Q^2 and high x , this fraction is small but increases with increasing Q^2 and decreasing x . For the lower x point at highest Q^2 , the contribution from beauty production is about 11% of that due to charm production. The contribution to the total cross section from $F_L^{c\bar{c}}$ calculated using the ZEUS NLO fit is, on average, 1.3% and at most 4.7% and is taken into account in the extraction of $F_2^{c\bar{c}}$. The size of the contribution from F_L is similar to that in other PDFs.

Cross sections in the measured D^* region and in the Q^2 and y kinematic bins were extrapolated to the full $p_T(D^*)$ and $\eta(D^*)$ phase space using HVQDIS. Typical extrapolation factors are between 4.7 at low Q^2 and 1.5 at high Q^2 . The extrapolation is affected by the following uncertainties:

- using AROMA fragmentation correction instead of the Peterson fragmentation yielded changes of typically less than 10% and up to 20%. Although these values are not very significant compared to the uncertainties in the data, the two corrections do produce a noticeable change in the shape of the cross section as a function of x . The most significant effects are in the highest x bins for a given Q^2 ;
- changing the charm mass by ± 0.15 GeV consistently in the HVQDIS calculation and in the calculation of $F_2^{c\bar{c}}$ leads to differences in the extrapolation of 5% at low x ; the value decreases rapidly to higher x ;
- using the upper and lower predictions given by the uncertainty in the ZEUS NLO PDF fit, propagated from the experimental uncertainties of the fitted data, to perform the extraction of $F_2^{c\bar{c}}$ gives similar values to the central measurement, with deviations typically less than 1%;
- changing the contribution of beauty events subtracted from the data gave an uncertainty of typically 2 – 3% and up to 10% at low x and high Q^2 .

These uncertainties were added in quadrature with the experimental systematic uncertainties when displayed in the figures. Extrapolating the cross sections to the full D^* phase space using the CTEQ5F3 proton PDF yielded differences compared to the ZEUS NLO QCD fit of less than 5% for $Q^2 > 11$ GeV² and less than 10% for $Q^2 < 11$ GeV².

The current data are shown in Fig. 6 compared with the previous measurement [1] and

with the ZEUS NLO QCD fit. The two sets of data are consistent³. The prediction describes the data well for all Q^2 and x . The uncertainty on the theoretical prediction is that from the PDF fit propagated from the experimental uncertainties of the fitted data. At the lowest Q^2 , the uncertainty in the data is comparable to the PDF uncertainty shown. This implies that the double-differential cross sections could be used as an additional constraint on the gluon density in the proton.

The values of $F_2^{c\bar{c}}$ are presented as a function of Q^2 at fixed values of x . The data compared with the ZEUS NLO QCD fit are shown in Fig. 7. The data rise with increasing Q^2 , with the rise becoming steeper at lower x . This demonstrates the property of scaling violation in charm production. The data are well described by the prediction.

Figure 8 shows the ratio $F_2^{c\bar{c}}/F_2$ as a function of x at fixed values of Q^2 . The values of F_2 used to determine the ratio were taken from the ZEUS NLO QCD fit at the same values of Q^2 and x at which $F_2^{c\bar{c}}$ is quoted. The ratio $F_2^{c\bar{c}}/F_2$ rises from 10% to 30% as Q^2 increases and as x decreases.

11 Conclusions

The production of D^* mesons has been measured in deep inelastic scattering at HERA in the kinematic region $1.5 < Q^2 < 1000 \text{ GeV}^2$, $0.02 < y < 0.7$, $1.5 < p_T(D^*) < 15 \text{ GeV}$ and $|\eta(D^*)| < 1.5$. The data extend the previous analysis to higher Q^2 and have increased precision.

Predictions from the AROMA MC underestimate, and those from the CASCADE MC overestimate, the measured cross sections. Predictions from NLO QCD are in reasonable agreement with the measured cross sections, which show sensitivity to the choice of PDF and hence the gluon distribution in the proton. The ZEUS NLO PDF, which was fit to recent inclusive DIS data, gives the best description of the D^* data. In particular, this is seen in the cross-section $d\sigma/d\eta(D^*)$. Further refinement of NLO QCD PDF fits may provide a gluon density leads to a better description of the data.

The double-differential cross section in y and Q^2 has been measured and used to extract the open-charm contribution to F_2 , by using the NLO QCD calculation to extrapolate outside the measured $p_T(D^*)$ and $\eta(D^*)$ region. Since at low Q^2 , the uncertainties on the data are comparable to those from the PDF fit the measured differential cross sections in y and Q^2 should be used in future fits to constrain the gluon density.

³ The first three points of the previous data were measured at $Q^2 = 1.8 \text{ GeV}^2$ and not 2 GeV^2 , so they have been shifted to 2 GeV^2 using the ZEUS NLO QCD fit. All other points were measured at the same Q^2 value.

Acknowledgments

The strong support and encouragement of the DESY Directorate have been invaluable, and we are much indebted to the HERA machine group for their inventiveness and diligent efforts. The design, construction and installation of the ZEUS detector have been made possible by the ingenuity and dedicated efforts of many people from inside DESY and from the home institutes who are not listed as authors. Their contributions are acknowledged with great appreciation. We thank J. Collins, B. Harris, G. Ingelman and R. Thorne for useful discussions.

References

- [1] ZEUS Coll., J. Breitweg et al., Eur. Phys. J. **C 12**, 35 (2000).
- [2] H1 Coll., C. Adloff et al., Phys. Lett. **B 528**, 199 (2002).
- [3] ZEUS Coll., J. Breitweg et al., Phys. Lett. **B 407**, 402 (1997).
- [4] H1 Coll., C. Adloff et al., Nucl. Phys. **B 545**, 21 (1999).
- [5] ZEUS Coll., S. Chekanov et al., Phys. Rev. **D 67**, 012007 (2003).
- [6] ZEUS Coll., U. Holm (ed.), *The ZEUS Detector*. Status Report (unpublished), DESY (1993), available on <http://www-zeus.desy.de/bluebook/bluebook.html>.
- [7] N. Harnew et al., Nucl. Inst. Meth. **A 279**, 290 (1989);
B. Foster et al., Nucl. Phys. Proc. Suppl. **B 32**, 181 (1993);
B. Foster et al., Nucl. Inst. Meth. **A 338**, 254 (1994).
- [8] M. Derrick et al., Nucl. Inst. Meth. **A 309**, 77 (1991);
A. Andresen et al., Nucl. Inst. Meth. **A 309**, 101 (1991);
A. Caldwell et al., Nucl. Inst. Meth. **A 321**, 356 (1992);
A. Bernstein et al., Nucl. Inst. Meth. **A 336**, 23 (1993).
- [9] A. Bamberger et al., Nucl. Inst. Meth. **A 382**, 419 (1996);
S. Magill and S. Chekanov, *Proceedings of the IX Int. Conference on Calorimetry (Annecy, Oct 9-14, 2000)*, B. Aubert et al. (ed.), p. 625. Frascati Physics Series 21 (2001).
- [10] A. Bamberger et al., Nucl. Inst. Meth. **A 401**, 63 (1997).
- [11] J. Andruszków et al., Preprint DESY-92-066, DESY, 1992;
ZEUS Coll., M. Derrick et al., Z. Phys. **C 63**, 391 (1994);
J. Andruszków et al., Acta Phys. Pol. **B 32**, 2025 (2001).
- [12] W.H. Smith, K. Tokushuku and L.W. Wiggers, *Proc. Computing in High-Energy Physics (CHEP), Annecy, France, Sept. 1992*, C. Verkerk and W. Wojcik (eds.), p. 222. CERN (1992). Also in preprint DESY 92-150B.
- [13] B.W. Harris and J. Smith, Phys. Rev. **D 57**, 2806 (1998).
- [14] V.N. Gribov and L.N. Lipatov, Sov. J. Nucl. Phys. **15**, 438 (1972);
L.N. Lipatov, Sov. J. Nucl. Phys. **20**, 94 (1975);
G. Altarelli and G. Parisi, Nucl. Phys. **B 126**, 298 (1977);
Yu.L. Dokshitzer, Sov. Phys. JETP **46**, 641 (1977).
- [15] B.W. Harris and J. Smith, Nucl. Phys. **B 452**, 109 (1995);
B.W. Harris and J. Smith, Phys. Lett. **B 353**, 535 (1995). Erratum, Phys. Lett. **B 359**, (1995) 423.

- [16] E. Laenen et al., Nucl. Phys. **B 392**, 162 (1993);
E. Laenen et al., Nucl. Phys. **B 392**, 229 (1993).
- [17] *Public access to ZEUS 2002 PDFs*, available on
<http://www-pnp.physics.ox.ac.uk/~cooper/zeus2002.html>.
- [18] C. Peterson et al., Phys. Rev. **D 27**, 105 (1983).
- [19] L. Gladilin, Preprint hep-ex/9912064, 1999.
- [20] P. Nason and C. Oleari, Nucl. Phys. **B 565**, 245 (2000).
- [21] H1 Coll., C. Adloff et al., Eur. Phys. J. **C 25**, 41 (2002).
- [22] ZEUS Coll., J. Breitweg et al., Eur. Phys. J. **C 6**, 603 (1999).
- [23] G. Ingelman and J. Rathsman, Comp. Phys. Comm. **101**, 135 (1997).
- [24] B. Andersson et al., Phys. Rep. **97**, 31 (1983).
- [25] H.L. Lai and W.K. Tung, Z. Phys. **C 74**, 463 (1997).
- [26] A. Chuvakin et al., Eur. Phys. J. **C 18**, 547 (2001).
- [27] R.S. Thorne, J. Phys. **G 25**, 1307 (1999).
- [28] R.G. Roberts and R.S. Thorne, Eur. Phys. J. **C 19**, 339 (2001).
- [29] H. Jung and G.P. Salam, Eur. Phys. J. **C 19** (2001).
- [30] CTEQ Coll., H.L. Lai et al., Eur. Phys. J. **C 12**, 375 (2000).
- [31] S. Catani, M. Ciafaloni and F. Hautmann, Nucl. Phys. **B 366**, 135 (1991).
- [32] L.V. Gribov, E.M. Levin and M.G. Ryskin, Phys. Rep. **100**, 1 (1983);
E.M. Levin and M.G. Ryskin, Phys. Rep. **189**, 267 (1990);
E.M. Levin et al., Sov. J. Nucl. Phys. **53**, 657 (1991);
E.M. Levin et al., Sov. J. Nucl. Phys. **54**, 867 (1991);
S. Catani, M. Ciafaloni and F. Hautmann, Phys. Lett. **B 242**, 97 (1990);
J.C. Collins and R.K. Ellis, Nucl. Phys. **B 360**, 3 (1991);
G. Marchesini and R.K. Webber, Nucl. Phys. **B 386**, 215 (1992).
- [33] S.P. Baranov et al., Eur. Phys. J. **C 24**, 425 (2002).
- [34] M. Ciafaloni, Nucl. Phys. **B 296**, 49 (1988);
S. Catani, F. Fiorani and G. Marchesini, Phys. Lett. **B 234**, 339 (1990);
S. Catani, F. Fiorani and G. Marchesini, Nucl. Phys. **B 336**, 18 (1990);
G. Marchesini, Nucl. Phys. **B 445**, 49 (1995).
- [35] T. Sjöstrand, Comp. Phys. Comm. **82**, 74 (1994).
- [36] H1 Coll., S. Aid et al., Nucl. Phys. **B 470**, 3 (1996).

- [37] A. Donnachie and P.V. Landshoff, Phys. Lett. **B 437**, 408 (1998);
 A. Donnachie and P.V. Landshoff, Phys. Lett. **B 470**, 243 (1999);
 A. Donnachie and P.V. Landshoff, Phys. Lett. **B 550**, 160 (2002);
 K. Golec-Biernat and M. Wüsthoff, Phys. Rev. **D 59**, 014017 (1999);
 A.V. Berezhnoy, V.V. Kiselev and A.K. Likhoded, Yad. Fiz. **63**, 1682 (2000);
 A.V. Berezhnoy, V.V. Kiselev and A.K. Likhoded, Phys. Rev. **D 62**, 074013 (2000);
 A.V. Berezhnoy and A.K. Likhoded, Yad. Fiz. **66**, 801 (2003);
 A.V. Kiselev and V.A. Petrov, Yad. Fiz. **60**, 1680 (1997).
- [38] S. Bentvelsen, J. Engelen and P. Kooijman, *Proc. Workshop on Physics at HERA*,
 W. Buchmüller and G. Ingelman (eds.), Vol. 1, p. 23. Hamburg, Germany, DESY
 (1992);
 K.C. Höger. (1992). Ibid. p. 43.
- [39] F. Jacquet and A. Blondel, *Proceedings of the Study for an ep Facility for Europe*,
 U. Amaldi (ed.), p. 391. Hamburg, Germany (1979). Also in preprint DESY 79/48.
- [40] U. Bassler and G. Bernardi, Nucl. Inst. Meth. **A 361**, 197 (1995).
- [41] ZEUS Coll., S. Chekanov et al., Eur. Phys. J. **C 21**, 443 (2001).
- [42] H. Abramowicz, A. Caldwell and R. Sinkus, Nucl. Inst. Meth. **A 365**, 508 (1995);
 R. Sinkus and T. Voss, Nucl. Inst. Meth. **A 391**, 360 (1997).
- [43] H. Jung, Comp. Phys. Comm. **86**, 147 (1995).
- [44] G. Marchesini et al., Preprint Cavendish-HEP-99/17 (hep-ph/9912396), 1999;
 G. Marchesini et al., Comp. Phys. Comm. **67**, 465 (1992).
- [45] A. Kwiatkowski, H. Spiesberger and H.-J. Möhring, Comp. Phys. Comm.
69, 155 (1992). Also in Proc. Workshop Physics at HERA, 1991, DESY, Hamburg.
- [46] R. Brun et al., GEANT3, Technical Report CERN-DD/EE/84-1, CERN, 1987.
- [47] M. Glück, E. Reya and A. Vogt, Z. Phys. **C 67**, 433 (1995).
- [48] L. Lönnblad, Comp. Phys. Comm. **71**, 15 (1992).
- [49] B.R. Webber, Nucl. Phys. **B 238**, 492 (1984).
- [50] K. Hagiwara et al., Phys. Rev. **D 66**, 010001 (2002).
- [51] S.D. Robins, *Charm production in deep inelastic scattering at HERA*. Ph.D.
 Thesis, University of Bristol, 2003. (unpublished).
- [52] M. Glück, E. Reya and A. Vogt, Eur. Phys. J. **C 5**, 461 (1998).
- [53] I. Redondo, *Charm electroproduction at HERA*. Ph.D. Thesis, Universidad
 Autónoma de Madrid, Report DESY-THESIS-2001-037, 2001.

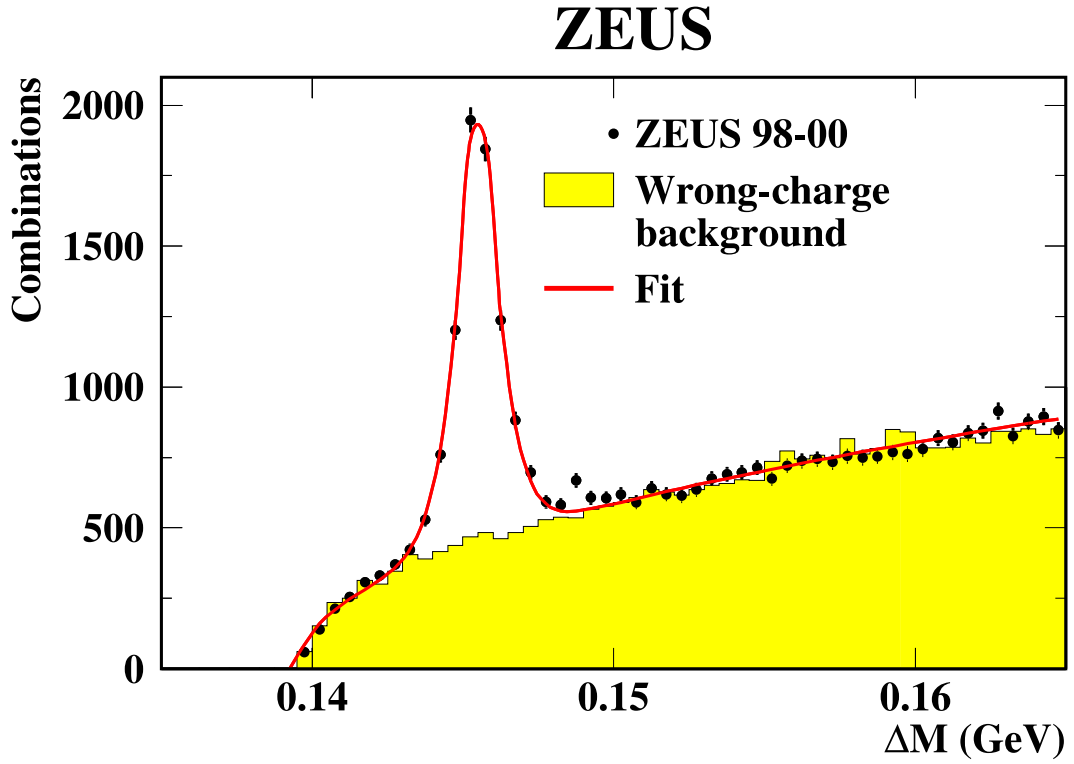


Figure 1: The distribution of the mass difference, $\Delta M = (M_{K\pi\pi_s} - M_{K\pi})$, for D^* candidates (solid dots). The ΔM distribution from wrong-charge combinations, normalised in the region $0.15 < \Delta M < 0.165$ GeV, is shown as the histogram. The solid line shows the result of the fit described in the text.

ZEUS

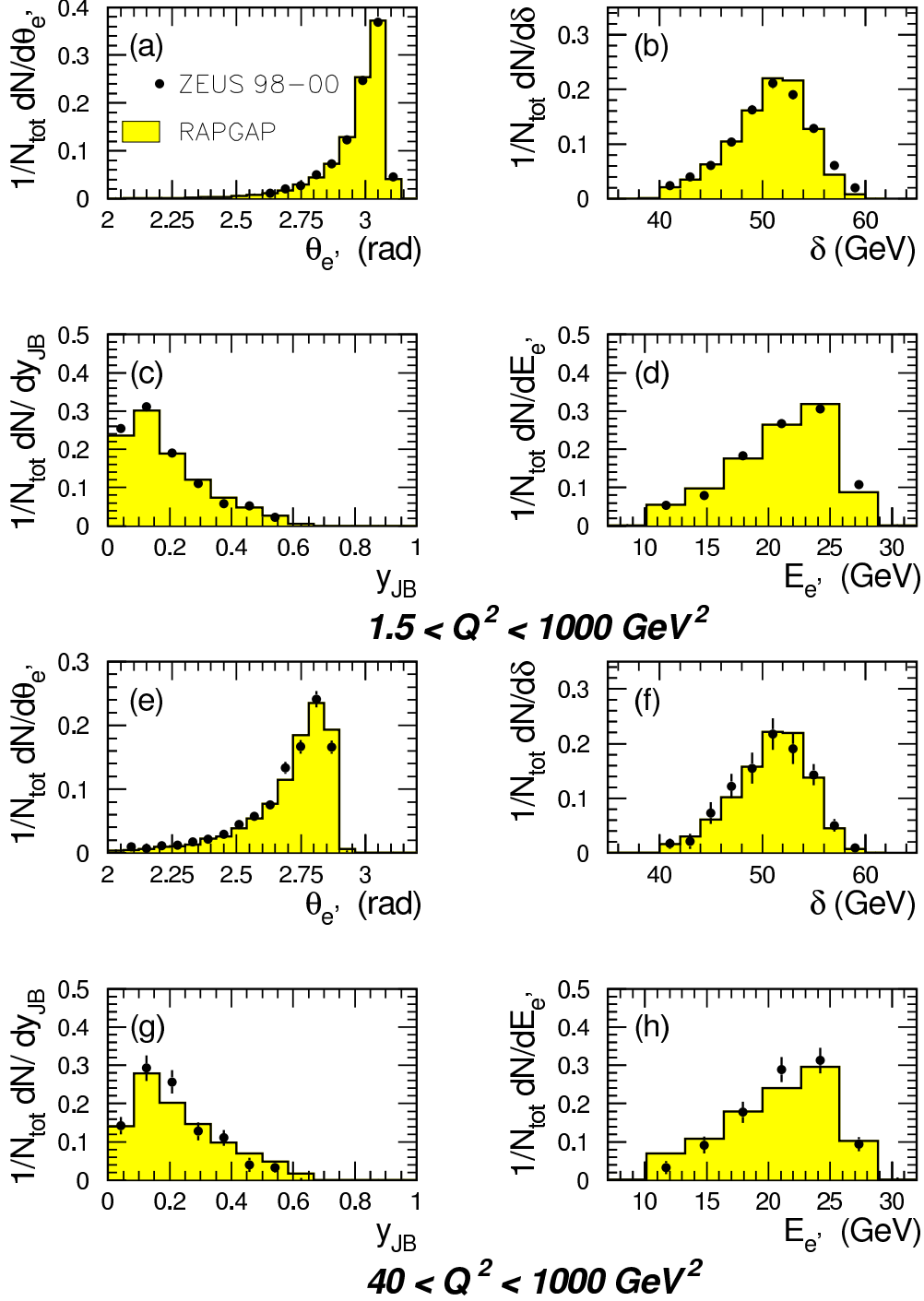


Figure 2: Reconstructed DIS variables for events with D^* candidates (after background subtraction) for data (points) compared to detector-level RAPGAP predictions (shaded histograms): (a)-(d) show the distributions for $1.5 < Q^2 < 1000 \text{ GeV}^2$, while (e)-(h) are the same distributions but for $40 < Q^2 < 1000 \text{ GeV}^2$. All histograms are normalised to unit area.

ZEUS

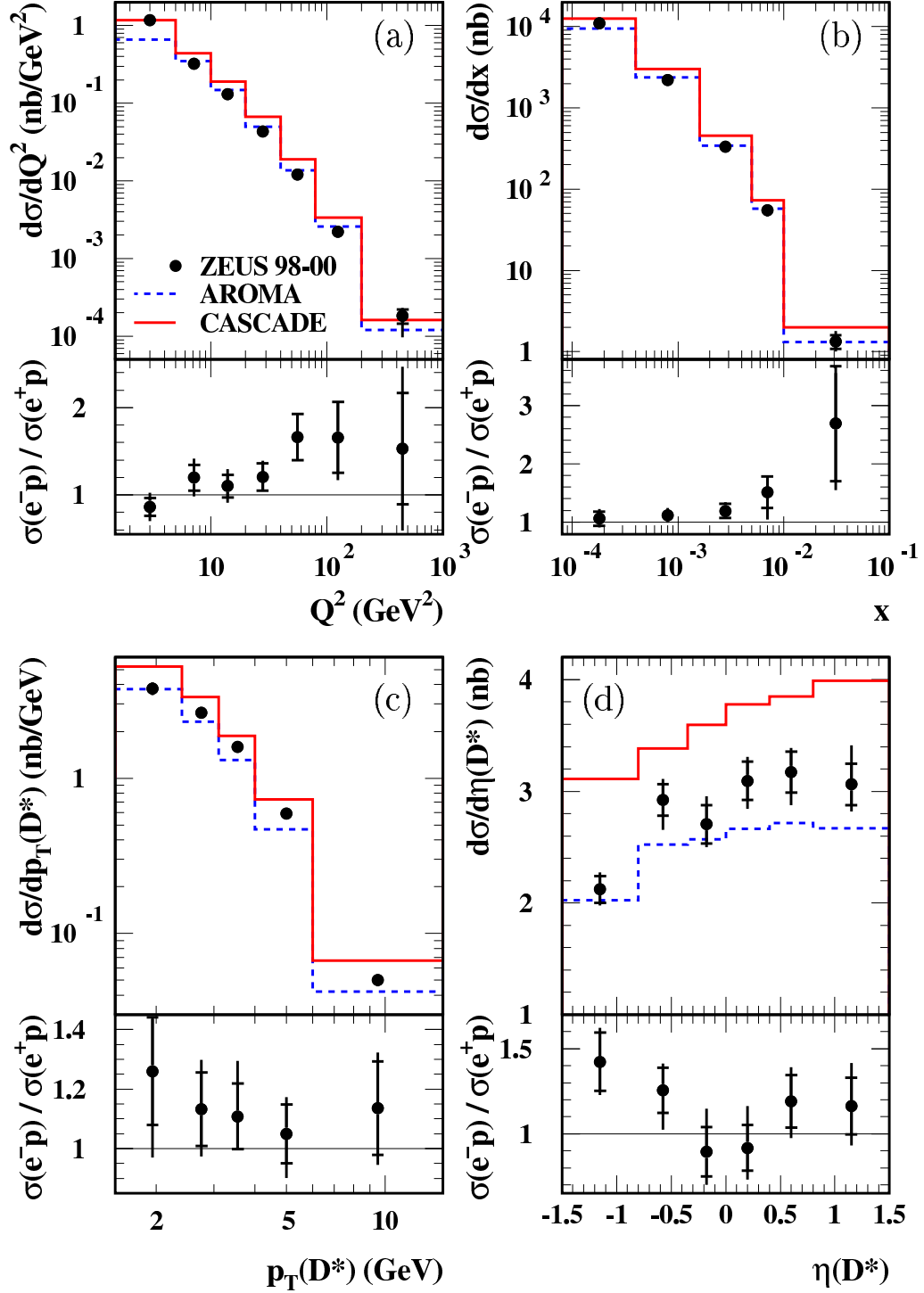


Figure 3: Differential D^* cross sections, for e^-p and e^+p data combined, as a function of (a) Q^2 , (b) x , (c) $p_T(D^*)$ and (d) $\eta(D^*)$ compared with MC predictions. The inner error bars show the statistical uncertainties and the outer bars show the statistical and systematic uncertainties added in quadrature. Predictions from the AROMA (dashed line) and CASCADE (solid line) MC programs are shown. The ratios of the cross sections for e^-p and e^+p data are also shown beneath each plot.

ZEUS

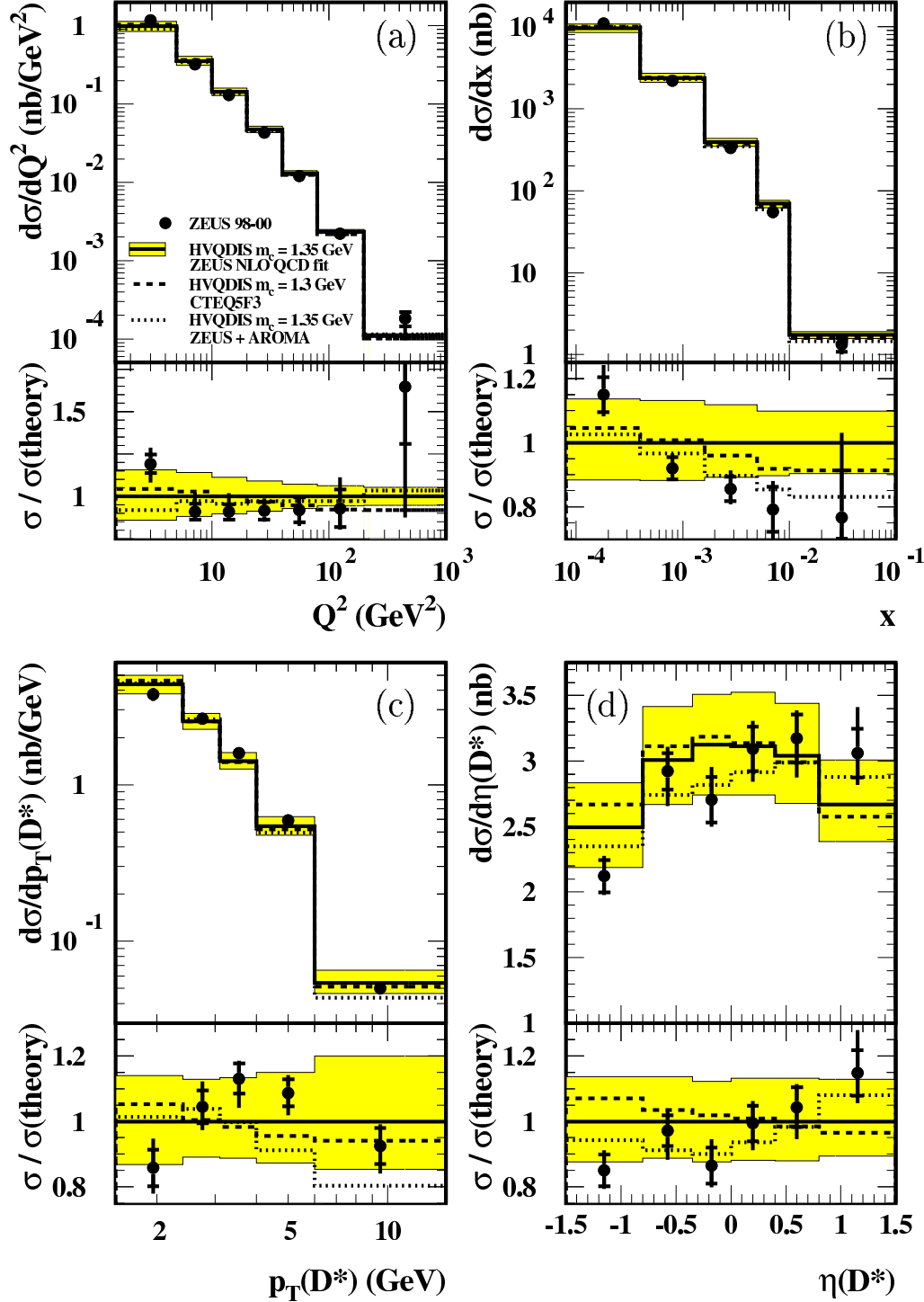


Figure 4: Differential D^* cross sections, for e^-p and e^+p data combined, as a function of (a) Q^2 , (b) x , (c) $p_T(D^*)$ and (d) $\eta(D^*)$ compared to the NLO QCD calculation of HVQDIS. The inner error bars show the statistical uncertainties and the outer bars show the statistical and systematic uncertainties added in quadrature. Predictions from the ZEUS NLO QCD fit are shown for $m_c = 1.35$ GeV (solid line) with its associated uncertainty (shaded band) as discussed in the text. Predictions using the CTEQ5F3 PDF (dashed-dotted line) and an alternative hadronisation scheme (dotted line) are displayed. The ratios of the cross sections to the central HVQDIS prediction are also shown beneath each plot.

ZEUS

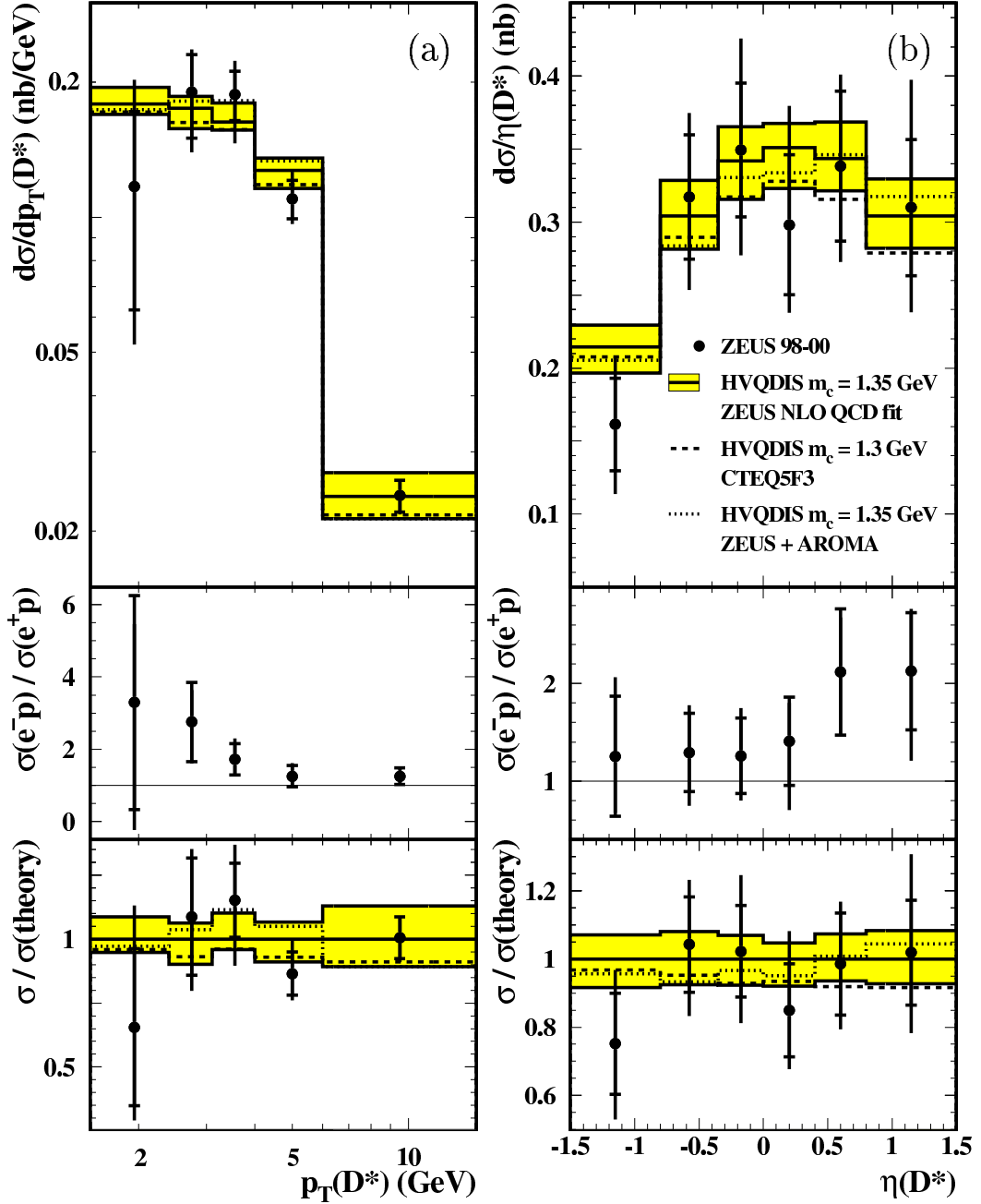


Figure 5: Differential D^* cross sections, for e^-p and e^+p data combined, as a function of (a) $p_T(D^*)$ and (b) $\eta(D^*)$ for $Q^2 > 40 \text{ GeV}^2$. The inner error bars show the statistical uncertainties and the outer bars show the statistical and systematic uncertainties added in quadrature. Predictions from the ZEUS NLO QCD fit are shown for $m_c = 1.35 \text{ GeV}$ (solid line) with its associated uncertainty (shaded band) as discussed in the text. Predictions using the CTEQ5F3 PDF (dashed-dotted line) and an alternative hadronisation scheme (dotted line) are displayed. The ratios of the cross sections for e^-p and e^+p data and for e^-p and e^+p data combined to the central HVQDIS prediction are also shown beneath each plot.

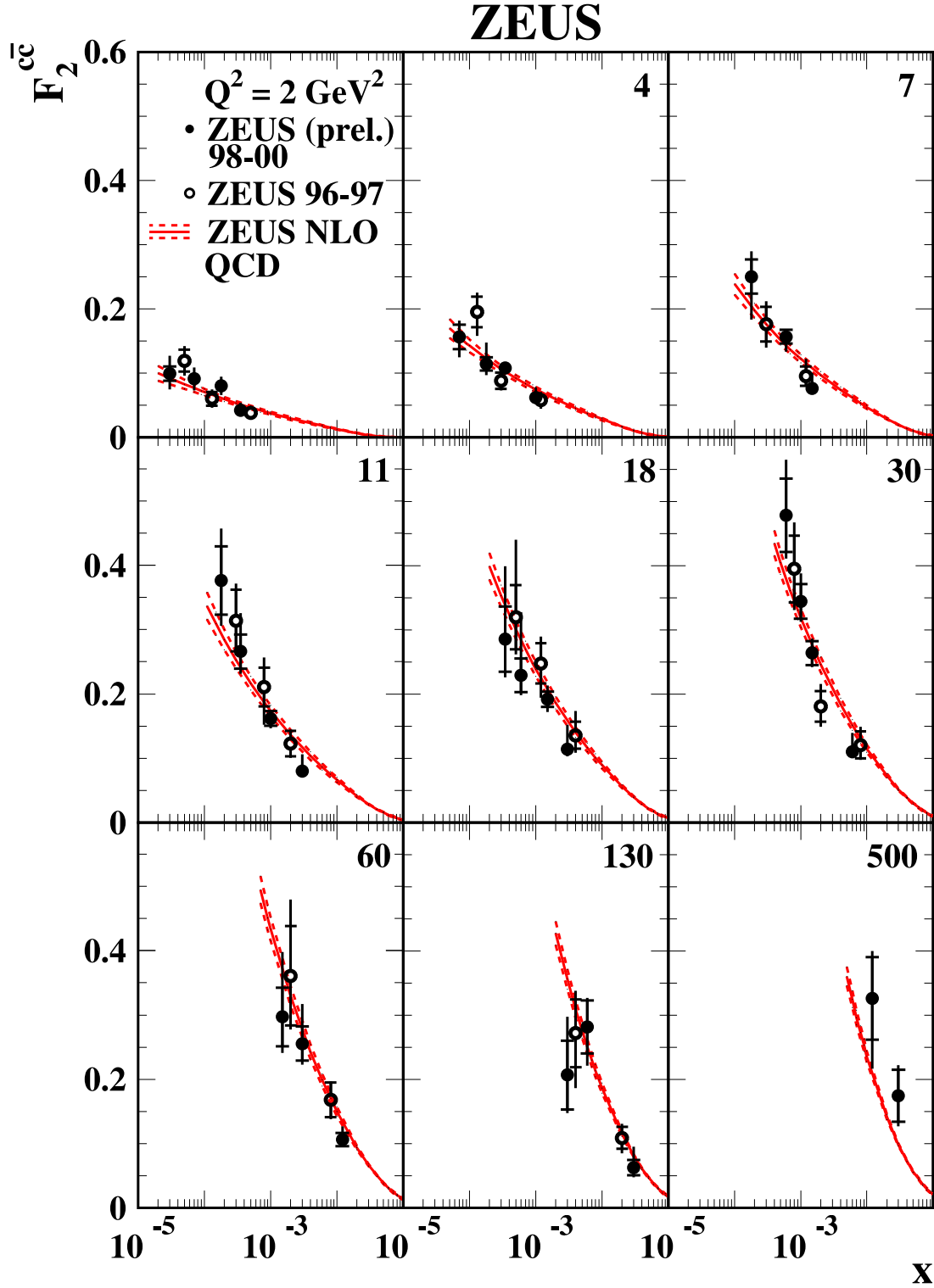


Figure 6: The measured F_2^{ce} at Q^2 values between 2 and 500 GeV^2 as a function of x . The current data (solid points) are compared with the previous ZEUS measurement (open points). The data are shown with statistical uncertainties (inner bars) and statistical and systematic uncertainties added in quadrature (outer bars). The lower and upper curves show the fit uncertainty propagated from the experimental uncertainties of the fitted data.

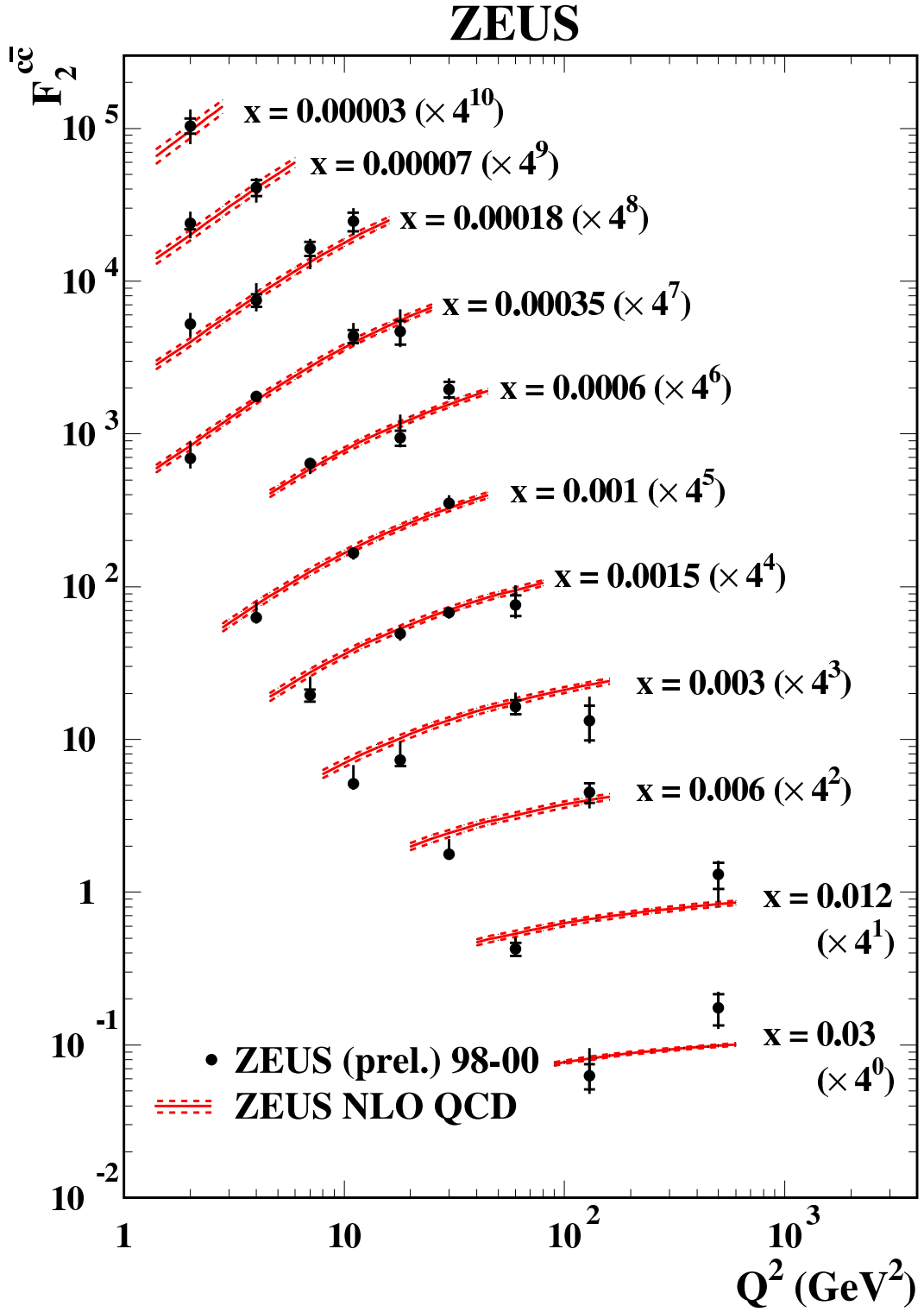


Figure 7: The measured F_2^{cc} at x values between 0.00003 and 0.03 as a function of Q^2 . The data are shown with statistical uncertainties (inner bars) and statistical and systematic uncertainties added in quadrature (outer bars). The lower and upper curves show the fit uncertainty propagated from the experimental uncertainties of the fitted data.

ZEUS

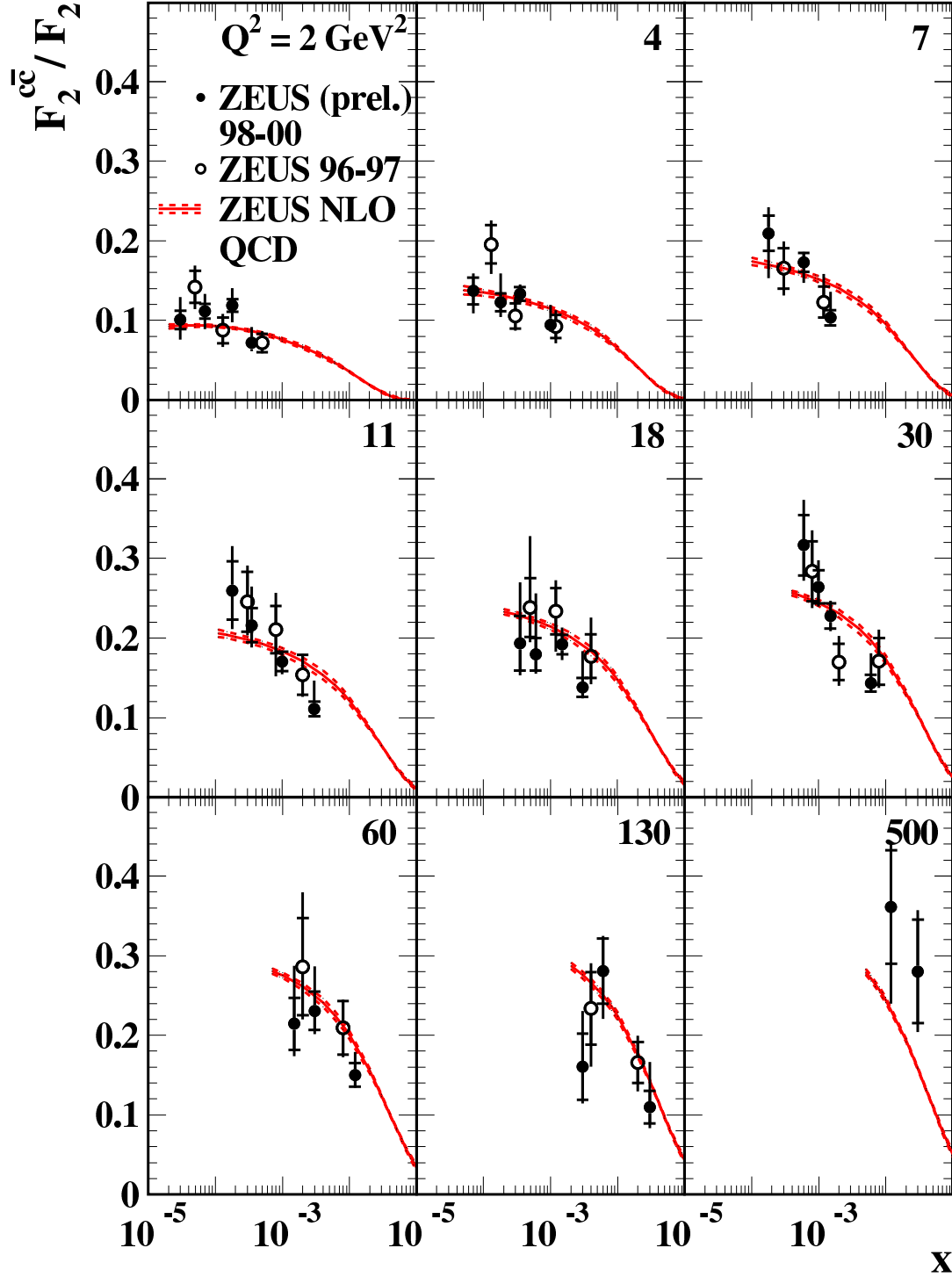


Figure 8: The measured ratio F_2^c/F_2 at Q^2 values between 2 and 500 GeV^2 as a function of x . The current data (solid points) are compared with the previous ZEUS measurement (open points). The data are shown with statistical uncertainties (inner bars) and statistical and systematic uncertainties added in quadrature (outer bars). The lower and upper curves show the fit uncertainty propagated from the experimental uncertainties of the fitted data.